Supplementary Information

High relative humidity as trigger for widespread release of ice nuclei

Timothy P. Wright[1], John D. Hader[1], Gavin R. McMeeking[2], and Markus D. Petters[1*]

[1]Department of Marine, Earth, and Atmospheric Sciences, North Carolina State University, Raleigh, North Carolina, 27695, USA.

[2]Droplet Measurement Technologies, Inc., Boulder, Colorado, 80301, USA

[*]Corresponding author: M. D. Petters

Introduction

This supplement is divided into five major sections. Sections 1 and 2 expound on the experimental methods for ice nuclei particles (INP) measurements and fluorescent measurements, respectively. Section 3 describes the measurement site and meteorological conditions. Section 4 presents extended results including data from the second case study and details about particle size distribution results from the ambient air measurements. Section 5 provides modelling results.

Section 1 - Ice nuclei concentration measurements

1.1 – Sample collection details

Ambient aerosol was sampled using a particle-in-liquid impinger (BioSampler manufactured by SKC, Inc.; Willeke et al. 1998). Ambient air is pulled through an inlet where it is directed towards an air-water interface in a collection well by three tangential orifices. The sample well holds 20 mL of ultra-pure water in which particles were collected upon impact with an efficiency of ~80% for particles $D = 200$ nm. The collection efficiency was ~100% for particles $1\ \mu m < D < 6\ \mu m$. For $D = 10\ \mu m$ the collection efficiency was ~50% (Willeke et al. 1998; Hader et al. 2014). Due to evaporation, the water level within the collection well decreased over time. To maintain high collection efficiency the flow through the impinger was stopped every hour and ultra-pure water was added to the system through the collection inlet. The addition of the water was expected to wash off large particles that impacted and adhered to the glass of the inlet. After three hours of operation a new collection vessel, filled with ultra-pure water, was placed on the impinger. While collecting the new sample, the sample water from the previous three hours of collection was processed in a drop freezing assay to measure the IN content (Section 1.2).

Rain water was collected by placing cleaned and baked Pyrex dishes on an elevated platform in an open area. The dishes remained covered with aluminum foil until just prior to the arrival of the precipitation. When precipitation stopped the collected water was transferred to clean glass bottles and placed in a refrigerator for up to 6 hours until the IN concentration within the rain water was measured.

1.2 – Drop freezing assay and IN concentration measurements

A drop freezing assay (Wright and Petters 2013; Wright et al. 2013; Hader et al. 2014) was used to measure the INP concentration in the impinger's sample collection water and collected rain water. Drops were emulsified in a hydrocarbon fluid to prevent dendrites created by freezing drops from inducing freezing in neighboring drops. The emulsion is placed on a hydrophobically coated glass slide that rested inside an aluminum dish. Drops were produced from the sample water in two distinct methods. The first method was to place 15 µL of sample water in 2 mL of squalene. This sample was vortexed to

produce water drops ranging in diameter from ~75 μm to 105 μm. The emulsion was then poured onto the glass slide. Drops produced in this method are referred to as *picodrops*. The second method produced larger drops and was accomplished by placing 2 mL of squalene directly on the slide and then, using a syringe, approximately ~150 nL (~650 μm in diameter) of sample water was placed in single drops in an array across the slide. Drops produced in this method are referred to as *nanodrops*. The dish, slide, and sample emulsion were placed in a sealed acrylic and polyoxymethylene chamber that was continuously flushed with dry nitrogen to prevent frosting. In the bottom of the chamber was an aluminum bridge with an embedded thermistor that acted to thermally connect the dish to a thermoelectric cooling system. The dish was cooled from -5 to -45 °C at a rate of 1 K min^{-1}. While cooling, an imaging system consisting of a 5 megapixel camera interfaced with a stereomicroscope recorded pictures at 0.1 Hz frequency. An automated algorithm analyzed the images and identified possible freeze events and calculated drop volumes from the image area. Subsequently, a user manually culled false positives from the freezing data. The resulting freezing spectra were inverted using the steps outlined in Hader et al. (2014) to determine the ambient IN concentration. Briefly, ambient IN concentration was calculated from the measured INP concentration in the liquid sample, the volumetric flow rate of the impinger sampler (12.5 L min^{-1}), the sampling time (~180 min), and subtracting the baseline INP concentration in the ultrapure water. Figure S1 and Figure S2 show the three-hour average ambient IN spectra as a function of temperature for both case studies. Crosses indicate the T = -15, -20, and -25 °C concentrations which are used to construct the time series data in other figures.
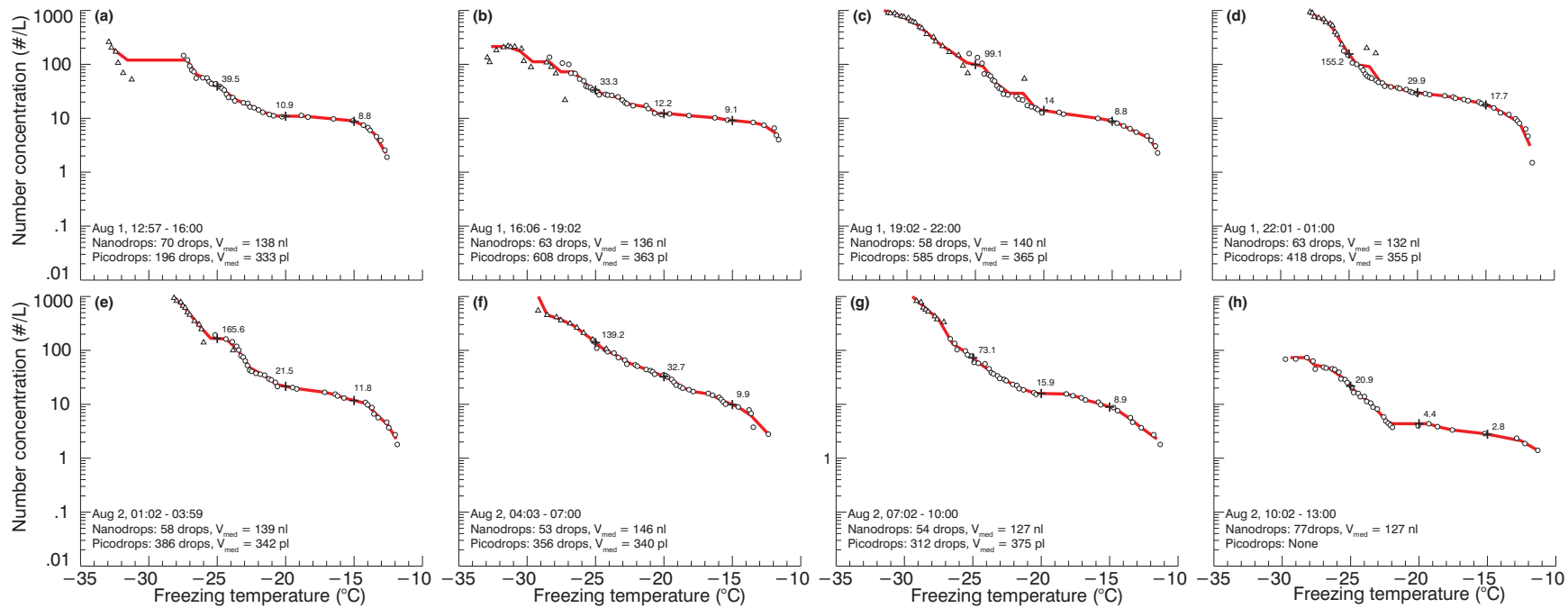
Figure S1. Each panel represents a three hour ambient IN spectra for August 1-2. Triangles and circles indicate picodrops and nanodrops, respectively. The red line corresponds to the running average concentration. Crosses and numbers indicate the concentration at $T = -15$, -20, and -25°C, which are reported in the figures of the main manuscript.
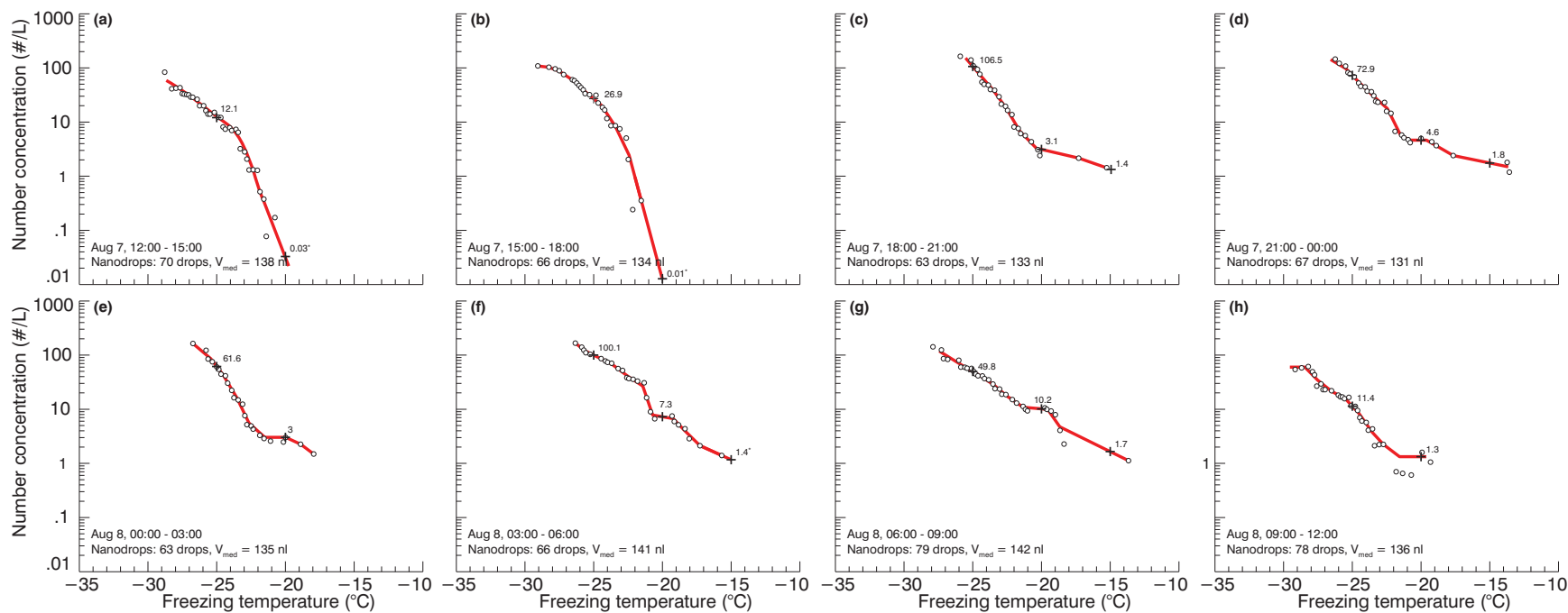
Figure S2. Each panel represents a three hour ambient IN spectra for August 7-8. The red line corresponds to the running average concentration. Crosses and numbers indicate the concentration at T = -15, -20, and -25°C, which are reported in the figures of the main manuscript. No nanodrop experiments are reported due to instrument malfunction.

Prior to sample retrieval, the refrigerated rain samples were vortexed for two minutes to minimize particle losses due to settling. Both pico- and nanodrop experiments were performed on the rainwater and IN concentrations in the rainwater are presented in Figure S3. Ice nuclei concentrations within the rain water were similar for the two showers. The number concentrations shown in Figure S3 are cumulative spectra and changes in slope indicate a mode in the probability density function. Specifically, the data show a population of particles that reaches peak INP activity between -11 and -15 °C.
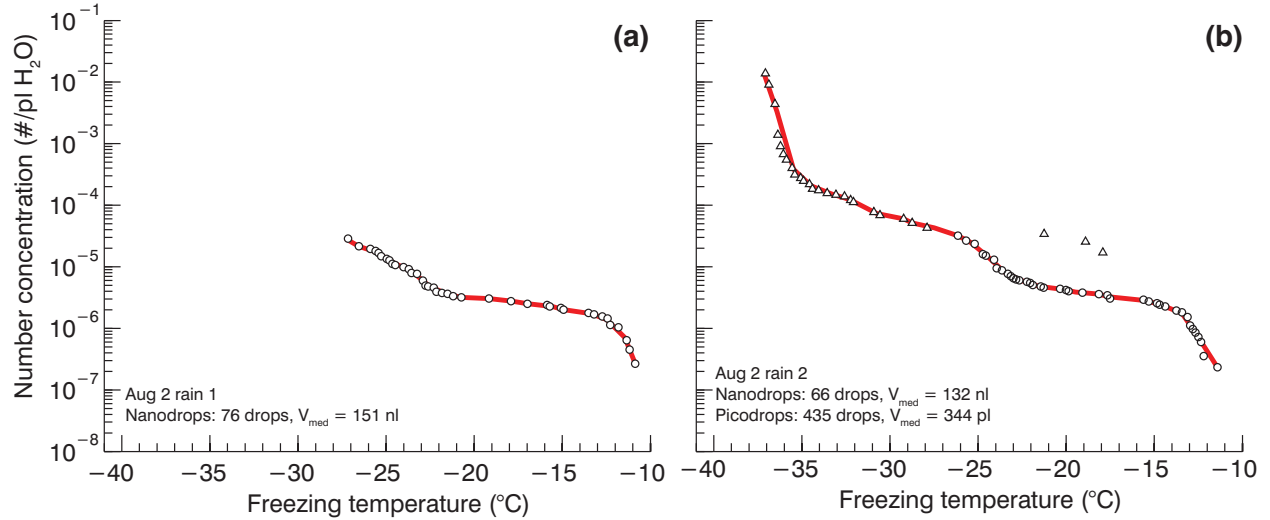

Figure S3. IN concentration in collected rainwater. Triangles and circles indicate picodrops and nanodrops, respectively. The red line corresponds to the running average concentration. No nanodrop experiment is reported in Figure S3a due to instrument malfunction.

1.3 – Estimated INP concentration in rainwater due to sweepout

The number of particles that is incorporated into the rainwater via sweepout depends on the volume swept by the raindrops. For monodisperse collecting drops and collected particles, the number of collected particles is

$$n_{coll} = \frac{\pi}{4}\left(D_p - d_p\right)^2 \left(V_t(D_p) - v_t(d_p)\right) E(D_p, d_p) n(d_p) t \tag{S1}$$

where D_p and d_p denote the collecting drop and collected particle diameters, V_t and v_t denote the fall velocities of the collecting drop and collected particle, $E(D_p, d_p)$ is the collection efficiency, $n(d_p)$ is the number concentration of the collected particles, and t is the time interval considered (Seinfeld and Pandis 2006). Assuming that a raindrop falls through a layer of thickness h, the time spent in the column is $t = h/V_t(D_p)$. The volume of the raindrop is $V_{drop} = \pi/6\, D_p^3$. Since $D_p \gg d_p$ the approximations $V_t \sim V_t(D_p) - v_t(d_p)$ and $D_p^2 \sim \left(D_p - d_p\right)^2$ are valid. Thus the number concentration of particles incorporated into the drop via sweepout is

$$c_s = \frac{n_{coll}}{V_{drop}} \sim \int \frac{3}{2} \frac{E(D_p, d_p) h}{D_p} \frac{dn(d_p)}{dd_p} dd_p \tag{S2}$$

where $dn(d_p)/dd_p$ is the particle size distribution function. The collection efficiencies are computed using the semi-empirical method of Slinn (1983) as described in Seinfeld and Pandis (2006), Wang et al. (2010), and Saleeby and van den Heever (2013). Equation (S2) demonstrates that concentration in the rainwater depends in principle on the three dimensional fields of rain and aerosol size distribution, the collection efficiency, and the thickness of the layer that the raindrops sweep. The rain and

IN size distribution as it varies through the layer is unknown. Rough estimates for c_s can be obtained by assuming a boundary layer height, raindrop diameters, and an INP number size distribution throughout the layer. Assuming that the INP number size distribution was identical to that of the FP3 particles (Figure S11), that the total concentration of FP3 particles throughout the layer is 100 L^{-1} and invariant with time, that 10% of the FP3 particles are active as INP at T = -15 °C, and that h = 1500 m (Section S3.2), Eq. S2 can be solved to estimate the concentration of INP in the rainwater. For D_p = 1, 2, and 5 mm raindrops, the calculated contribution of INP from sweepout c_s was 14, 6, and 1.2% of the observed INP (3×10^{-6} pl^{-1}, Figure S3). Note that the raindrop size distribution was unknown, but the rain was heavy which suggests that the majority of the raindrops exceeded 1 mm in size. Since it is assumed that the collected particles are distributed uniformly through the layer and that the number concentration does not decrease with time due to removal, the latter two assumptions represent a "worst case scenario", likely biasing the estimated contribution from sweepout high. Nonetheless, the calculations are approximate since wet removal is highly non-linear with size. The collection efficiency of larger particles (d_p > 3 μm) is much higher than the collection efficiency of smaller particles because inertial impaction dominates over the contribution to efficiency by interception (cf. Fig. 1, Wang et al., 2010). The majority of the FP3 particles had d_p < 3 μm, but we do not know the distribution of INP efficiency with size. We suggest that in our case study the contribution from sweepout to the measured INP in rainwater was likely less than 10%, but underscore the need for future studies to perform size-resolved measurements of the INP within collected rainwater to firmly exclude the possibility that sweepout plays a major role.

Assuming sweepout is negligible, a very approximate relationship between ambient INP concentrations and rainwater concentration is 1 IN L^{-1} (air) = 10^{-5} pl^{-1} rainwater (Hader et al., 2014), suggesting that the cloud-level INP concentrations of the -11 and -15 °C range may have exceeded 0.1 L^{-1} (100 m^{-3}) air.

Section 2 - Fluorescent measurements

The Wideband Integrated Bioaerosol Sensor (WIBS-4A; DMT, Inc.) is a fluorescence spectrometer that measures single particle size and UV fluorescence (Kaye et al. 2005; Robinson et al., 2013; Huffman et al. 2013). Particle size is inferred based on the side scattered intensity from the particle's passage through a 633 nm diode laser beam. The particle is then exposed to UV light at 280 and 370 nm and fluorescence is detected in the bands of 310 to 400 nm and 400 to 600 nm. This produces fluorescence signals in three channels: channel F1 (excitation 280 nm/emission 310-400 nm), channel F2 (excitation 280 nm/emission 400-600 nm), and channel F3 (excitation 370 nm/emission 400-600 nm). The fourth channel (excitation 370 nm/emission 310-400 nm) is discarded due to saturation of the detector by elastic scattering of the 370 nm UV light.

The UV fluorescence signals presented here are often associated with the presence of biological particles that contain fluorophores such as tryptophan and NAD(P)H (Després et al. 2012; Huffman et al. 2012). Although a particle may fluoresce at a given excitation and emission pair, it does not necessarily imply that the particle contains the above fluorophores. One class of possible non-biological interferents would be polycyclic aromatic hydrocarbons (PAH). These occur in the atmosphere primarily in the gas-phase as products of incomplete combustion, absorbed on organic aerosol particles, or as semi-volatile species present in both gas and particle phases (Pöhlker et al. 2012). PAHs are known to be highly fluorescent, especially in the spectral band that corresponds to the WIBS "tryptophan" channel (Kumke et al. 1995). PAHs can be enriched on soot particles from biomass burning and fuel combustion, however it is unlikely combustion particles were measured with the WIBS as the particle concentrations were independent of nearby human activity (e.g. rush hour) and WIBS analysis of car exhaust produced no discernable fluorescence signal. The atmospherically suspended PAH molecules would be undetectable by the WIBS instrument as these are smaller than the 0.5 μm cut off and therefore would not trigger the instruments xenon lamps. Additionally, PAH coatings on organic aerosols produce only weak fluorescent

emissions due to efficient quenching by bulk material (Lewitzka and Niessner 1995; Panne et al. 2000). Therefore the strong F1 signal for the FP3 particles likely comes from a source other than PAH. Another source of non-biological fluorescence interference would be dust suspended in the atmosphere. We tested a dust proxy (Arizona Test Dust) and found it to have a very weak to no fluorescence signature in any of the channels. In addition, it is unlikely that windblown dust contributed to the ambient fluorescence signal since there was no major dust source upwind. Humic-like substances (HULIS) are a final possible source for non-biological fluorescing particles. HULIS is a mixture of heterogeneous compounds formed by the natural decay and oxidation of biological material (Graber and Rudich 2006). Fluorescence of HULIS substances has been observed in several spectral positions including the F1/tryptophan channel of the WIBS (Pöhlker et al. 2012). Fluorescence signals from the WIBS could be from HULIS particles suspended in the air as there is no way to differentiate these from biological particles. However, terrestrial sources are generally not considered to be the source of bulk HULIS in atmospheric aerosol (Graber and Rudich 2006). While we term particles in the FP3 group as "tryptophan like", tryptophan is not the only biological fluorophore that can be detected in the F1 channel. Examples of other biological fluorophores that have relatively high absorption coefficients for 280 nm excitation with a non-zero quantum yield are riboflavin and flavin adenine dinucleotide (FAD) (Hill et al. 2013). However, the signal from these fluorophores will be weak and would likely register low in intensity in the F1 channel. In summary and agreement with previous studies, non-biological particles producing fluorescing artifacts within the WIBS instrument are rare for particles larger than 0.5 µm and any such interferents would likely only exhibit a weak signal that is below the classification for the FP3 particles which this study focuses on (Huffman et al. 2010; Pöhlker et al. 2012; Després et al. 2012).

The WIBS-4A returns size data in micrometers for particles in the size range of 0.5 to 15 micrometres and the fluorescence signal strength is returned in arbitrary units in the scale of 0 to ~2000 for each channel. Particle concentrations from the WIBS-4A were determined from the flow rate through the instrument and binned into 5 min segments. Following Gabey et al. (2010) a baseline fluorescence signal value was determined for each channel due to low-level excitation of the optical components in the WIBS-4A. This baseline value was measured by measuring fluorescent emissions following excitation of the cavity in the absence of particles. This measured the fluorescence of an empty sensing volume for a total of ten minutes during the August 7-8 case study. Baseline intensity in each channel is normally distributed. To identify the difference between weakly fluorescing and non-fluorescing particles, a baseline excitation threshold ($E_{threshold}$) was established:

$$E_{threshold} = <E_{baseline,i}> + 2.5\sigma_i. \qquad (S3)$$

In Eq. (S3), $<E_{baseline,i}>$ is the modal baseline value for channel i, and σ_i is the standard deviation of the signal counts at each fluorescing value (Gabey et al. 2010). For this study, the threshold values for each channel were: $F1_{threshold} = 162$, $F2_{threshold} = 96$, and $F3_{threshold} = 13$. These threshold values were then subtracted from all values prior to signal analysis.

Visual analysis of the WIBS-4A fluorescence data was used to designate five regions in the three dimensional space created by the three fluorescence channels. Figure S4 shows a visualization of the WIBS-4A fluorescing data. Each point in the figure represents a 50x50x50 a.u. binning of the data. Fraction of particles in each bin is indicated by the warmth of the colors.

Each particle was grouped into a common fluorescence excitation and emission profile (EEP). Criteria for selecting EEP boundaries involved analysis of the distribution of particles in each channel and how merging groups of like particles together impacts the concentration of particles for any newly formed EEP. For example, the value of 1900 was selected to split channel F1 because it is the minimum bin value along that channel axis and the merging of the FP3 and FP4 EEP did not produce a group of particles whose concentration significantly deviated from that of FP3. Furthermore, small deviations from these somewhat subjective borders do not affect the relative changes in FP3 particles with RH for the case

studies. Seven characteristic EEPs are defined: FP1 through FP5, fluorescing biological aerosol particles (FBAPs), and fluorescing particles (FP). Thresholds defining these groups are listed in Table S1. FBAPs are a previously defined class of particles that fluoresce in channels F1 and F3, but not F2 (Toprak and Schnaiter, 2013). We note that our visual grouping is based only on the relative strengths of the F1, F2, and F3 channels and does not factor in size.
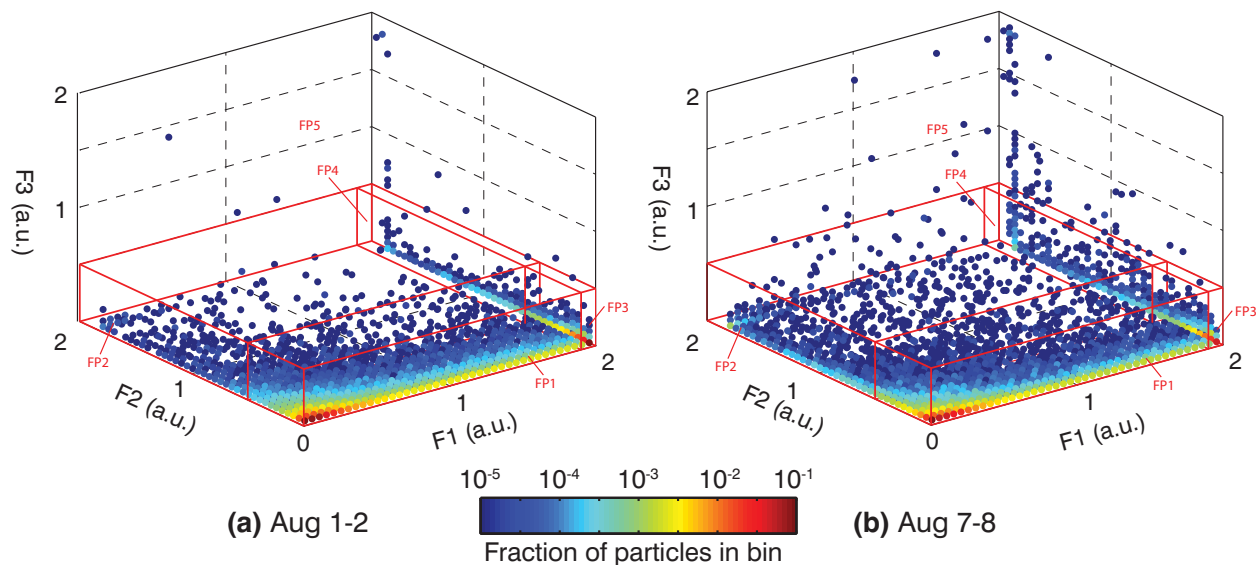

(a) Aug 1-2   Fraction of particles in bin   **(b)** Aug 7-8

Figure S4. Frequency distribution of the three WIBS-4A fluorescence channels. The value on each axis corresponds to the intensity reported by the WIBS-4A divided by 1,000 and is in arbitrary units. Colors denote the fraction of particles that fall within a cube that is 0.05 a.u. on an edge. No symbol is drawn for empty cubes. Red lines demark excitation-emission profile regions FP1 to FP5. Panels (a) and (b) are for total particles sampled during the August 1-2 and August 7-8 measurement periods, respectively.

Table S1: Fluorescence excitation-emission profile (EEP) values. Values are given in arbitrary units. FP particles must fluoresce > 0 in at least one of the three channels.

	F1 range		F2 range		F3 range
FP1	0 – 1900	AND	0 – 500	AND	0 – 500
FP2	0 – 1900	AND	500 – 2000	AND	0 – 500
FP3	1900 – 2000	AND	0 – 500	AND	0 – 500
FP4	1900 – 2000	AND	500 – 2000	AND	0 – 500
FP5	0 – 2000	AND	0 – 2000	AND	500 – 2000
FBAP	>0 – 2000	AND	0	AND	>0 – 2000
FP	>0 – 2000	OR	>0 – 2000	OR	>0 – 2000

Figure S4 shows that the majority of the fluorescing particles were located in the zero axis point (weakly fluorescing in all channels) and the corner of the 3D space that is fluorescing strongly in channel F1 and weakly in channels F2 and F3. The majority of particles that fluoresced in channel F2 were classified in FP4. FP5 particles constitute the smallest fraction of particles measured. A full summary of the breakdown on the fraction of particles that are classified in each group is given in Table S2. Included in this table are counts of total particles (n_{total}) and particles that fluoresced in any channel ($n_{fluorescence}$).

Table S2: Number statistics. Rows 1-5, denote the percentage of fluorescing particles identified in each group. Row 6 is the total number of particles detected by the WIBS-4A and row 7 is the total number of particles that fluoresced.

	Aug 1 – 2	**Aug 7 – 8**
FP1	91.7 %	95.2 %
FP2	0.5 %	1.6 %
FP3	7.5 %	2.9 %
FP4	0.3 %	0.3 %
FP5	0.1 %	0.1 %
n_{total}	619,107	705,748
$n_{fluorescence}$	267,887	283,703

Section 3 – Measurement site and meteorological conditions

3.1 – Site details

Measurements were made on the roof of Jordan Hall, a five story building, which is located on the campus of North Carolina State University (NCSU). The NCSU campus is located approximately 3 km west of the city center of Raleigh, NC, USA. Raleigh is located in the east-central portion of North America and the climate is temperate and humid. Throughout the city and surrounding the building are numerous forests comprised of a mix of hardwood (primarily oak and hickory) and pine species (LeGrand and Wiecek 2003). The rooftop of the building stands ~1-5 meters above the canopy height. On a tower approximately 4.5 meters above the collection site is a meteorological station that is operated by the State Climate Office of North Carolina. This station includes a standard instrument package that returns measurements of temperature, pressure, relative humidity, and wind speed.

3.2 – Relationship between boundary layer structure, particle fluxes, and emissions

Here we briefly address the question of whether the observed increase in nocturnal INP and FP3 concentrations is likely due to active emissions from the surface or if it could be explained by other processes. In principle, concentrations may not be a reliable proxy of the intensity or the net direction of the flux. For example, the growth of a well-mixed boundary layer via entrainment may decrease concentrations at the surface even in the presence of a net influx of particles. The daytime radiosonde profiles from Greensboro, NC indicate that during both the Aug 1-2 and Aug 7-8 measurement cycles, a well-mixed layer ~1.5 km deep was present during the daytime sounding. The height of the nocturnal boundary layer during the evening of Aug 1-2 was estimated to be ~0.4 km, as determined from the nighttime sounding. We point out that the decoupling of the residual well-mixed layer from surface influences and the formation of a stable nocturnal boundary layer will not change particle concentrations in either layer if there is no net flux. In general, however, in the presence of a shallow stable layer, a net particle flux from the surface into the boundary layer will result in a larger concentration increase when compared to the same flux of particles into a deeper layer, due to the smaller effective volume of the layer. If accumulation of particles due to a net flux from the surface into the boundary layer occurs overnight, the concentration of particles at the surface may decrease in the morning when the nocturnal boundary layer and residual well-mixed layer rejoin to form a convective mixed layer.

Nonetheless, the observations suggest that indeed a net particle flux was active overnight. Observations show an increase in FP3 and INP throughout the night as the nocturnal boundary layer was present and likely deepening. Non-fluorescent particle concentrations measured by the WIBS during Aug 1-2 did not show the same trends, suggesting that the dynamics of non-fluorescing and fluorescing aerosol was different. We point out here that aerosol volumes do not undergo systematic diurnal changes

in the summertime boundary layer in the Southeastern U.S. (e.g. Nguyen et al. 2014 Figure A1), which is consistent with the notion that boundary layer dynamics alone are unlikely to explain observed concentration changes.

3.3 – Length scales and synergistic effects

The hypothesized RH driven emission scenario requires that emissions occur ahead of the frontal sweep. The speed of the arriving front was ~30 km hr^{-1}. The RH increase started ~6 hr before the arrival of the front and the increase in RH was caused partially by prefrontal cooling and partially by nocturnal cooling. The RH deviated from the typical diurnal cycle ~4 hr ahead of the precipitation providing an estimate of the length/time scale of the prefrontal fetch of 120-180 km. The characteristic time scale for lateral shear diffusion can be estimated as $t = ~h/u_*$ (Elder 1959), where h is the depth of the fluid and u_* is the friction velocity. For conditions during the Aug 1-2 case we estimate from the nearby sounding that the height of stable nocturnal boundary layer was ~$h = 400$ m and calculated u_* varied between 0.1 and 0.4 m/s throughout the night[1]. The time scale required to mix particles to the sampling height of ~23 m (1-5 m above canopy height) via shear diffusion was between 1 and 4 min. For reference, a 400 m deep layer with $u_* = 0.2$ m/s has a characteristic mixing time scale of 33 min. In dynamic equilibrium, increases in concentration with time are the result of a net flux into the system (cf. Eq. 1, Lighthart and Shaffer, 1994). We argue, to a first approximation, that the observed increase in concentration is due to a distributed source with a footprint on the order of several 10s of km and that we sampled air from a reasonably mixed stable boundary layer. It is important to point out that this analysis is highly approximate. Fundamentally the evidence presented in this work is based on correlation and cannot establish causation. Actual flux measurements are needed to determine the intensity and scale of emissions. Furthermore, the conceptual simplified picture in Figure 1 does not account for a number of likely important meteorological effects, including boundary layer evolution and stability, temporary mixing of the stable and residual layer during night time (Salmond and McKendry 2005), mesoscale frontal circulations (Young and Johnson 1984), the location and the strength of prefrontal precipitating cells, the height of the lifting condensation and the freezing level, and the interplay between diurnal heating profiles and frontal passages. The sum of these will determine the overall prefrontal fetch and determine the relative importance of the release of IN and their impact on precipitation.

3.4 – Case Study 1, Aug 1-2, 2013

Weather systems over North Carolina generally move from west to east. The large scale weather systems that were in place during the August 1-2 measurement period are shown in Figure S5a with the location of Raleigh, NC indicated by the red marker along the eastern seaboard. Ambient conditions for this twenty-four hour period were largely influenced by the passage of a cold front. The temperature initially peaked midday and then started declining slowly towards sunset. This trend continued until the arrival of the frontal boundary ~1:30 local time (LT), August 2. A new air mass moved into the area at this time, evidenced by the sharp drop in mixing ratio and equivalent potential temperature, θ_e (Figure S5c). Wind speeds gusted up to ~5.5 m s^{-1} with the strongest winds occurring right before the first rainband passed. Subsequently, the atmospheric conditions remained relatively constant throughout the rest of the night. A second rainband passed near sunrise (~6:00 LT). After sunrise the temperature rose while the relative humidity steadily decreased.

---

[1] The measured wind velocity was decomposed into u and v components. The u component was used to verify that there is general agreement between the derived turbulent kinetic energy (TKE) and values found from NCEP reanalysis (Mesinger et al 2004). The variance of the u component was then used to estimate u_* (Banta et al. 2006).
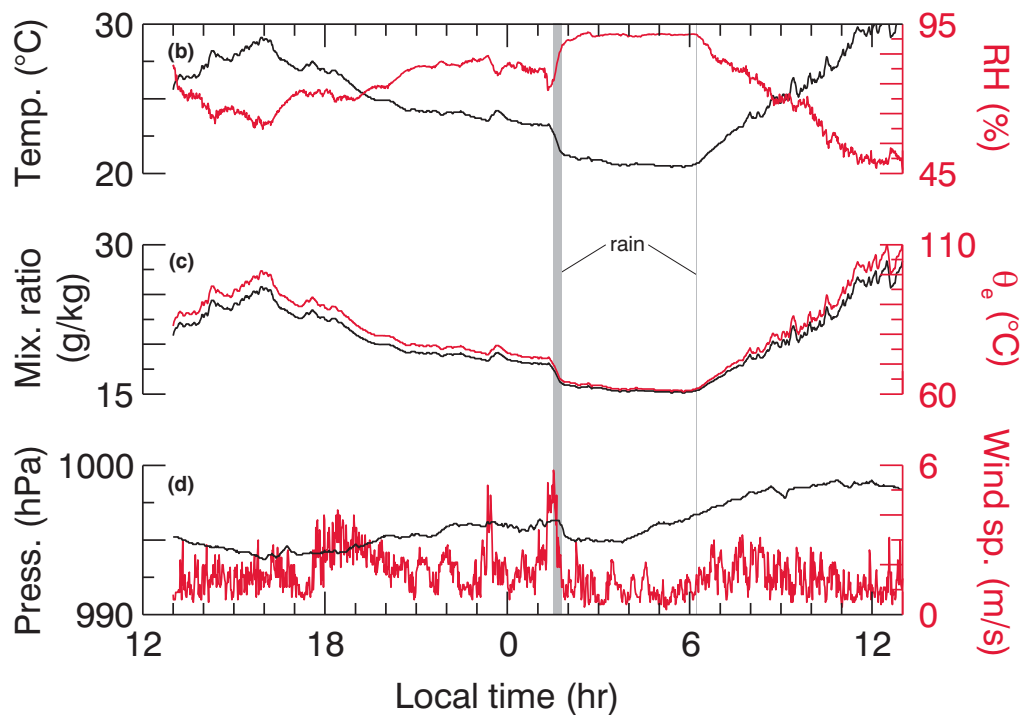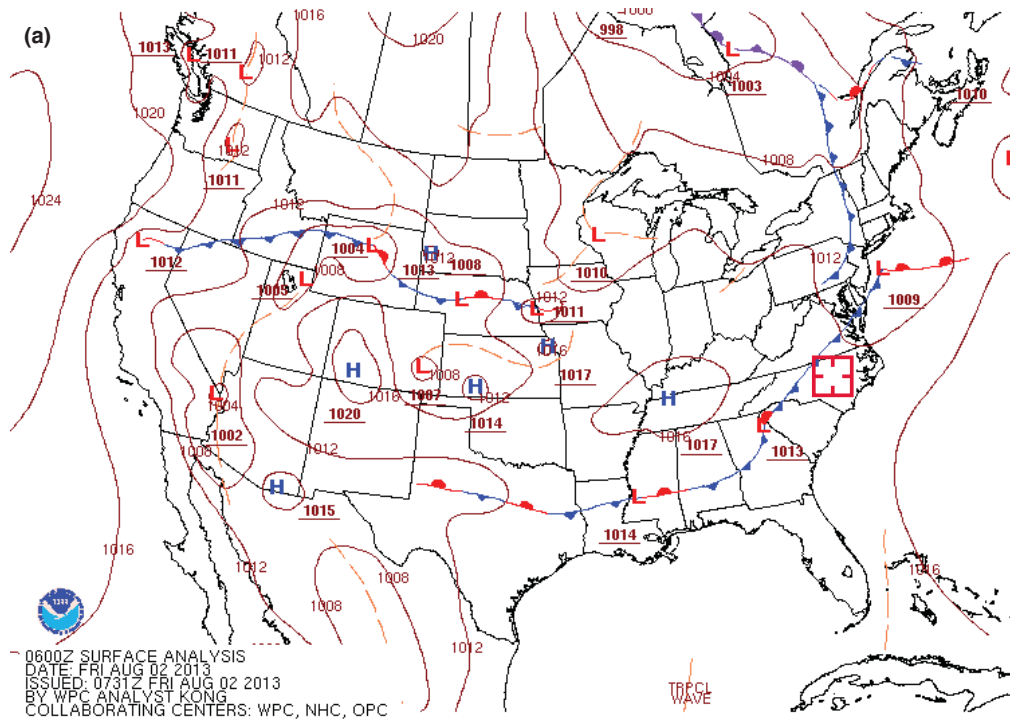
Figure S5. (a) Conditions on August 1-2, 2013 as reported by the National Weather Service across the continental US. The red marker along the east coast shows the location of the measurement site. Meteorological conditions at the site: (b) Measured temperature (black) and relative humidity (red). (c) Calculated mixing ratio (black) and equivalent potential temperature (red). (d) Measured pressure (black) and wind speed (red). Grey shaded areas indicate precipitation times.

<u>3.5 – Case Study 2, Aug 7-8, 2013</u>

The weather for the August 7-8 measurement cycle was characterized by a stationary high over central NC (Figure S6a) with the surface pressure remaining nearly constant at 1000 hPa. At noon on August 7 the temperature was 29 °C, where it remained throughout the late afternoon. During this time the INP concentration at all three temperatures and FP3 concentration was relatively low (Figure S7). The INP concentration for $T = $ -15 and -20 °C dropped to below the detection limit (~0.8 L^{-1}) approaching sunset, while the INP concentration at $T = $ -25 °C and FP3 concentration increased slightly. From sunset to close to sunrise, the temperature dropped steadily to 22 °C. During the first half of the night the concentration of IN at all temperatures increased with a significant increase in the concentration of IN active at $T = $ -25 °C. The INP concentration at all three reported temperatures decreased noticeably during the midnight to 03:00 measurement period. FP3 particle concentrations slowly rose throughout the night with a sharp decrease at sunrise in conjunction with the decrease in RH. After sunrise, the temperature increased to 30 °C by the end of the measurement cycle. The relative humidity, which was primarily driven by the temperature, increased from ~45% to ~90% between noon on August 7 and sunrise on August 8 at which point it dropped quickly throughout the morning to ~50%.
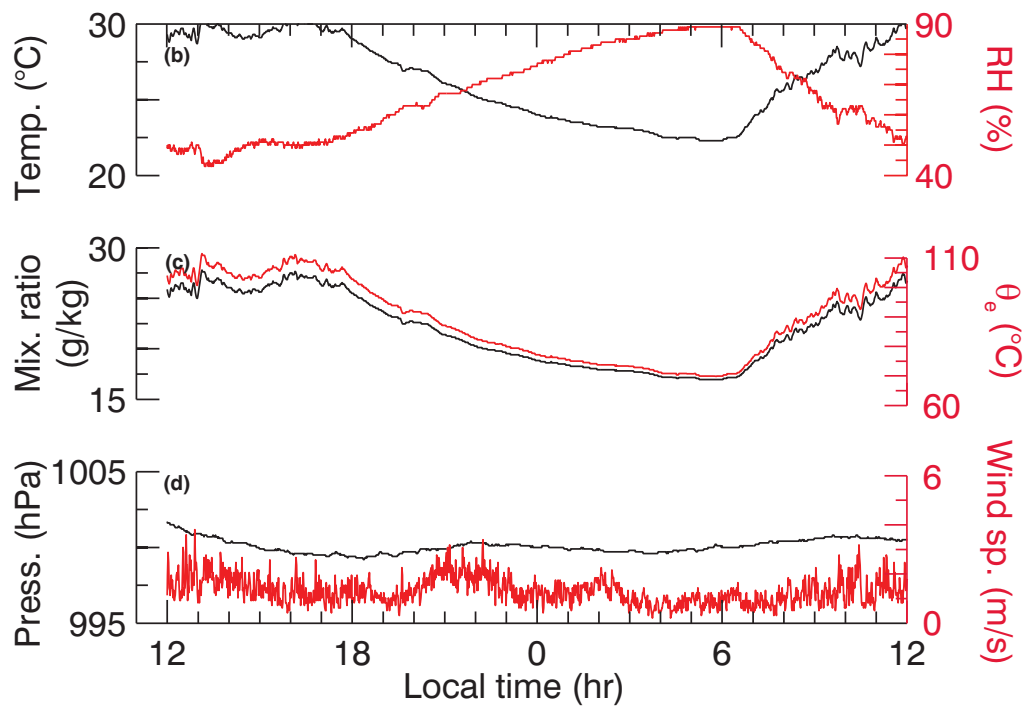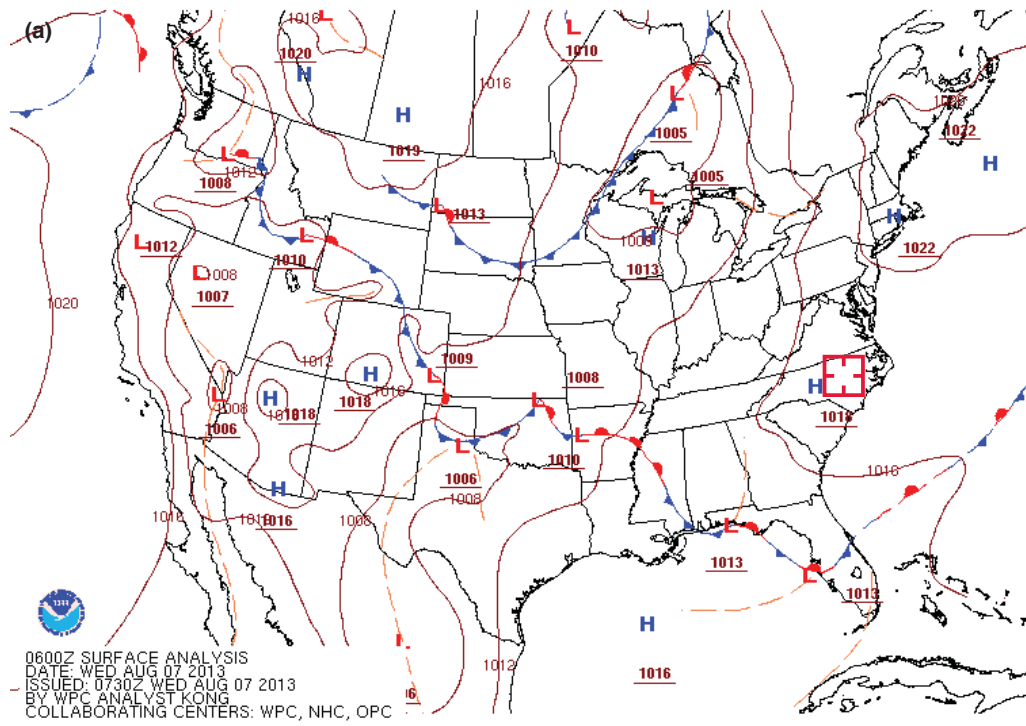
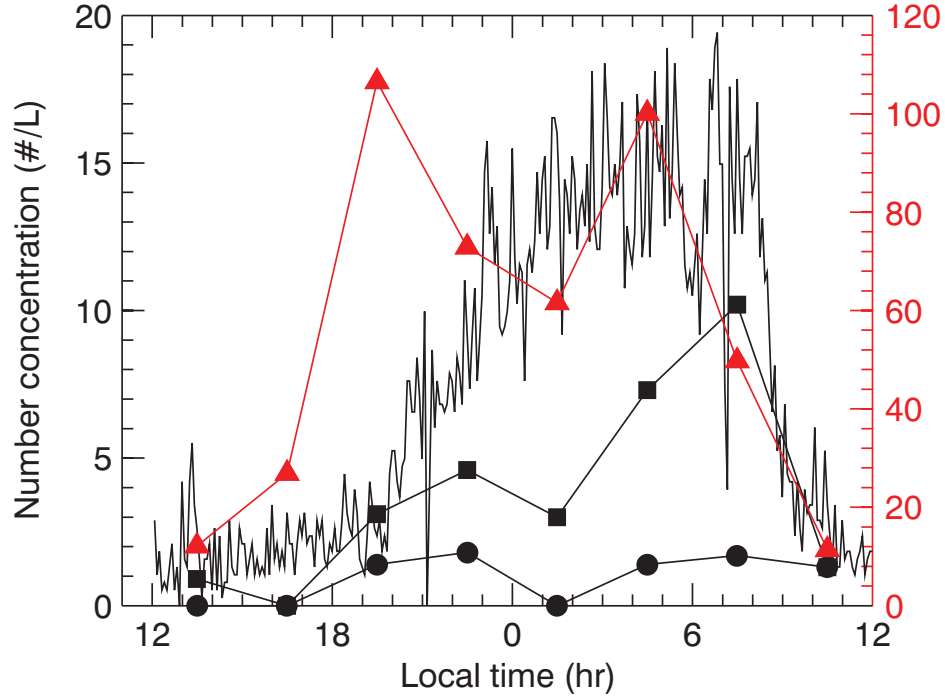**Figure S6**. Same as Figure S5 for August 7-8, 2013.

Figure S7. FP3 fluorescent particle number concentrations (black line) over 24 hours starting at August 7, 12:00 LT. Ambient IN concentration at T = -15, -20, and -25 °C are represented by circles, squares, and triangles, respectively. Red and black colors map to the red and black ordinal axes respectively.

Section 4 – Additional results

Scatterplots of INP, FBAP, FP, and FP3 concentrations vs RH are presented in Figures S8 and S9 for the August 1-2 and August 7-8 case studies, respectively. Correlation coefficients between RH and all fluorescent particle and FBAP concentrations were lower than the correlation coefficient between RH and FP3 particle concentration for both case studies. The Pearson correlation coefficient between the three hour averaged FP3 particle concentration and IN concentration was highest for IN active at T = -20 °C with R^2 = 0.71 and 0.64 for the Aug 1-2 and Aug 7-8 case studies, respectively. The correlation coefficients are summarized in Table S3.

Table S3: Summary of the Pearson correlation coefficients presented in Figures S8 and S9. Each entry corresponds to the correlation coefficient between the listed parameter and RH.

	Aug 1-2	**Aug 7-8**
INP concentration at T = -15 °C	0.48	0.24
INP concentration at T = -20 °C	0.78	0.6
INP concentration at T = -25 °C	0.82	0.34
FBAP concentration	0.17	0.55
FP concentration	0.31	0.7
FP3 concentration	0.56	0.82

Figure S10 presents scatter plots of IN with various fluorescent particle proxies. For the August 1-2 measurement period, FBAP concentrations had the weakest predictive power on INP concentration. FP3 concentrations had the highest correlation with R^2 = 0.71 and 0.70 for T = -20 and -25 °C, respectively. The correlation between INP concentrations and fluorescing particle concentrations was

14

weaker for the August 7-8 measurement cycle with no significant difference between FBAP and FP3 particles. The correlation coefficients between FBAP and FP3 concentrations was also high for both measurement cycles (R^2 = 0.72 and 0.8 for Aug 1-2 and Aug 7-8, respectively). This suggests the source for FBAP and FP3 could be the same. The highest correlation existed between IN active at T = -20 °C across all fluorescing particle categories with R^2 values between 0.64 and 0.71.

Figure S11 summarizes the size distribution for the total particle concentration, FP, and FP3 concentration for August 1-2 and August 7-8 case studies. The majority of the FP3 particles were in the 2 – 6 µm size range for both measurement cycles. This peak was more pronounced when the set of particles was expanded to include all fluorescing particles. The fraction of total particles that fluoresce (FP) approaches 100% for particles with $D > 3$ µm. Notably, the fraction of total particles that fluoresced in group FP3 shows a distinct maximum at $D \sim$ 3-6 µm, highlighting that the FP3 size distribution is decoupled from the total fluorescence and total particle size distribution. This further suggests that the FP3 particle may have a distinct source.
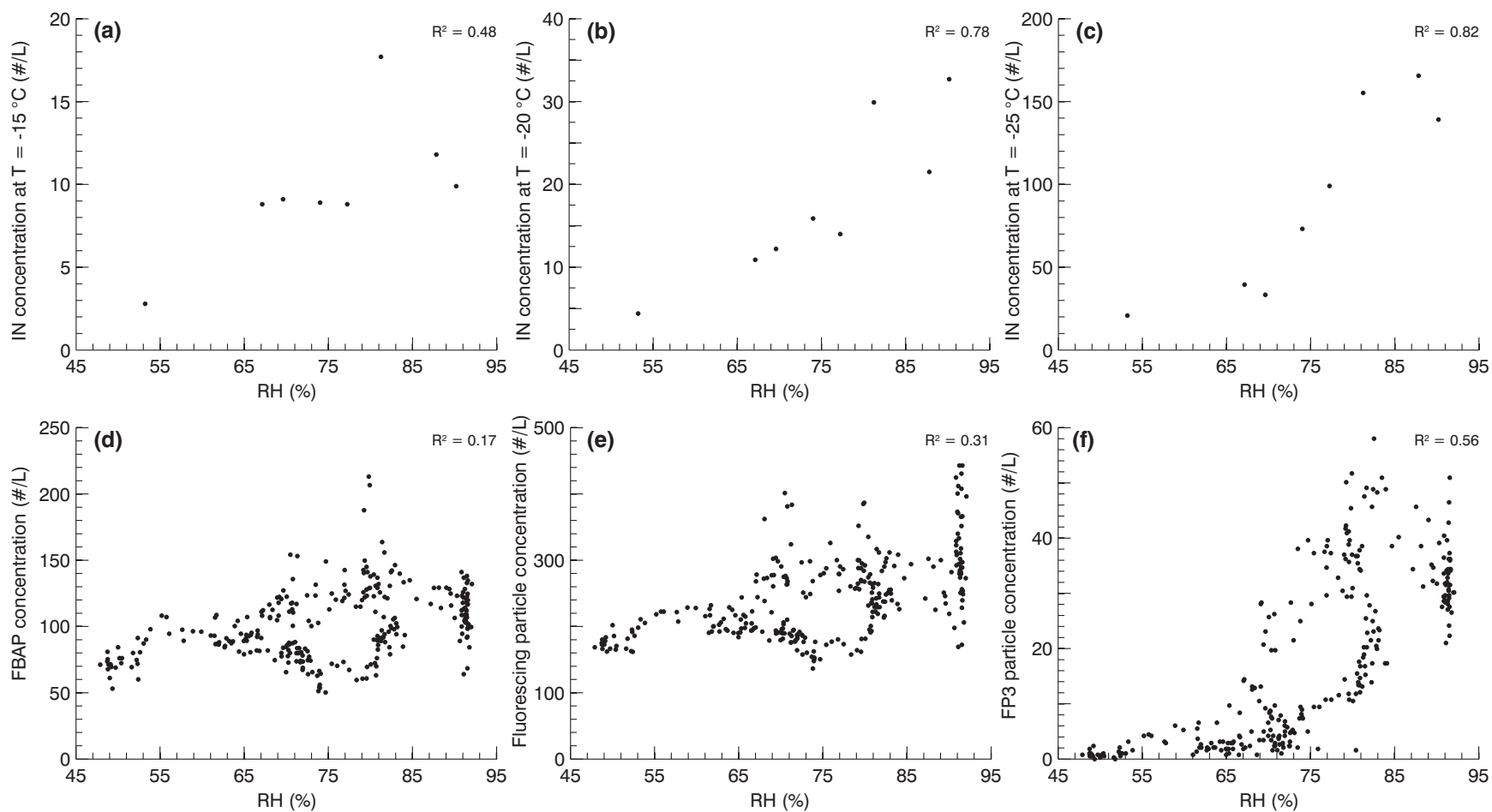
Figure S8. Correlation plots for the August 1-2 case study. Scatterplot comparison between three hour average of RH and IN concentration active at (a) T = -15 °C, (b) T = -20 °C, and (c) T = -25 °C. Correlation plots between RH and (d) FBAP particle concentration, (e) total fluorescing particle (FP) concentration, and (f) FP3 particle concentration.
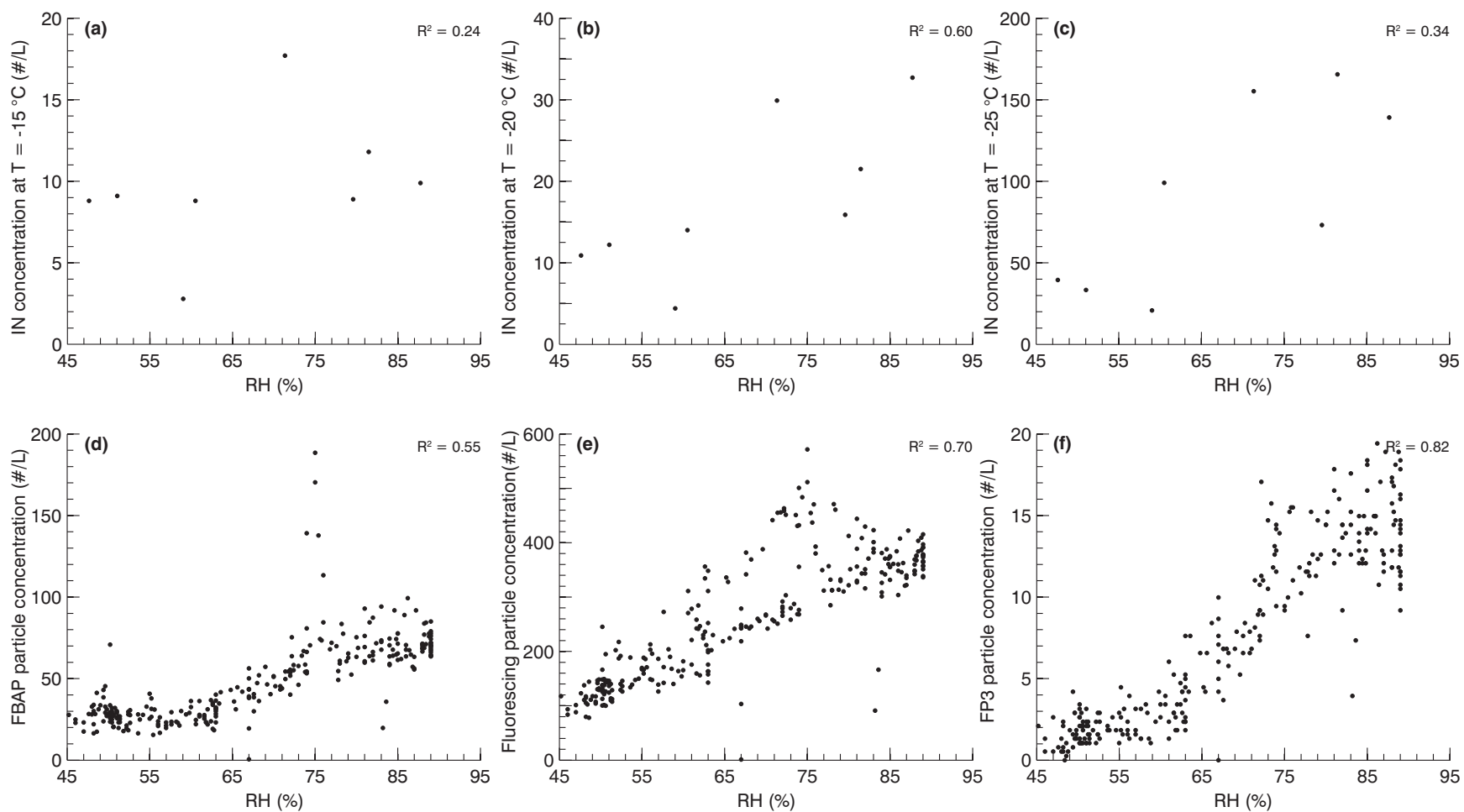
Figure S9. Correlation plots for the August 7-8 case study. Panels are the same as those in Figure S7.
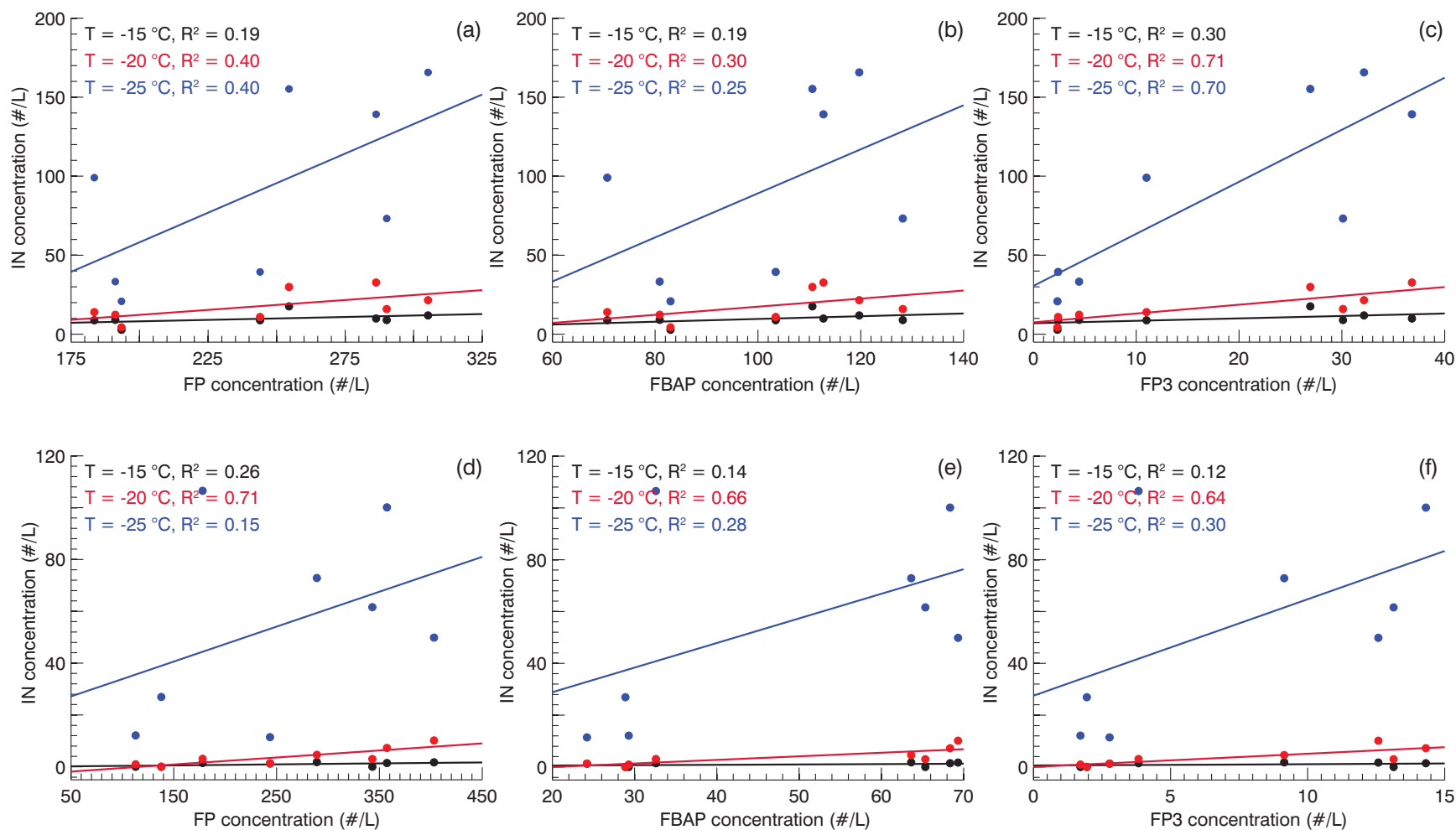
Figure S10. Scatterplots showing the correlation of IN concentration at T = -15, -20, and -25 °C with FP (a,d), FBAP (b,e), and FP3 (c,f) particle concentrations. The correlation coefficient for each temperature compared to the specific fluorescence particle category is shown in the upper left of each panel. Top row is for the August 1-2 case study and bottom row is for the August 7-8 case study.
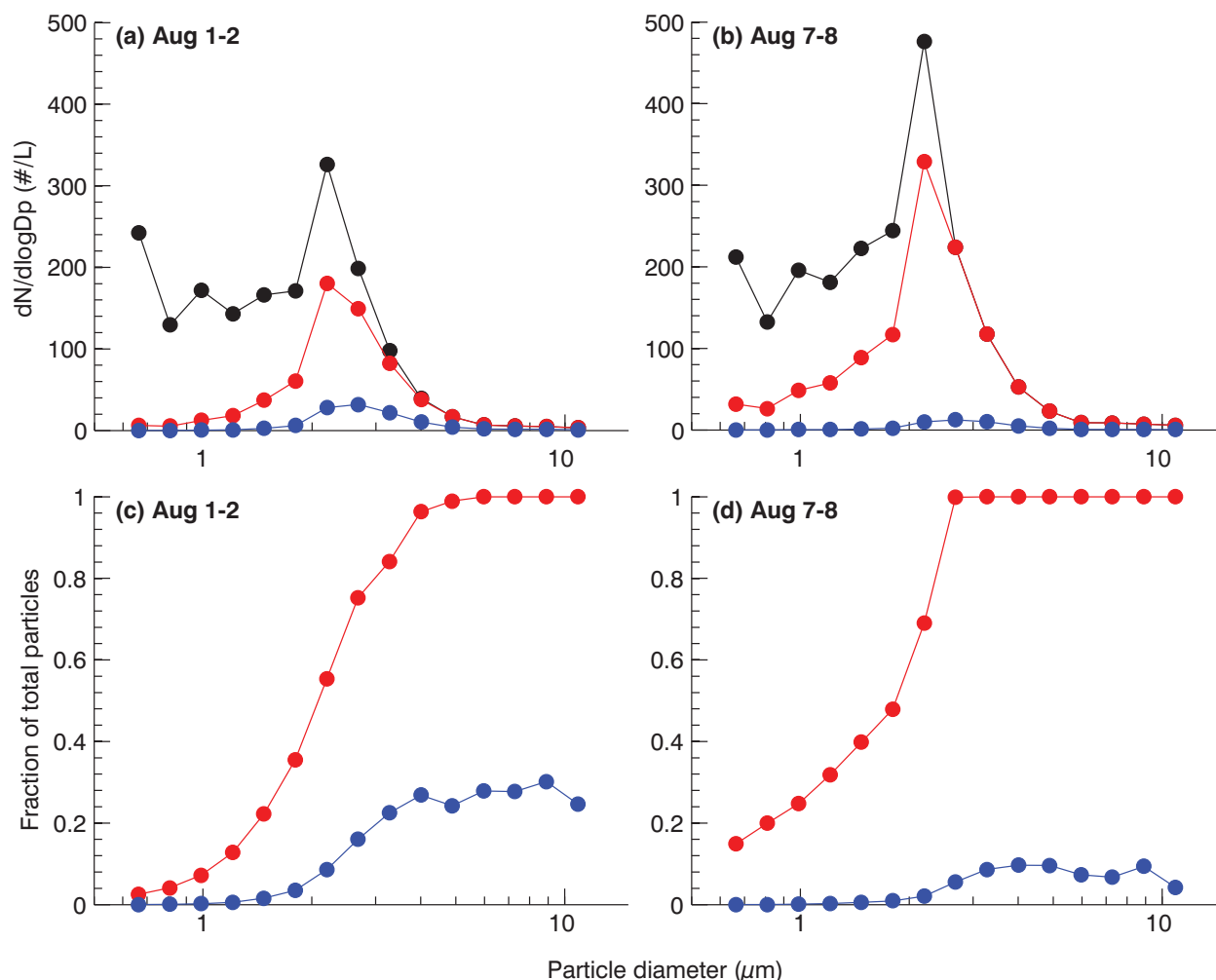
Figure S11. Top panels: Size distribution for all particles measured during the (a) August 1-2 measurement period and (b) August 7-8 measurement period. The total particle concentration (black), total fluorescing particle (FP) concentration (red), and FP3 fluorescing particle concentration (blue). Bottom panels: Fraction of total particles that fluoresced in any channel (red) and fraction of total particles that fluoresced in FP3 (blue) for (c) August 1-2 measurement period and (d) August 7-8 measurement period.

Section 5 – Model predictions

Eq. (1) in DeMott et al. (2010) and Eq. (3) in Tobo et al. (2013) was used in conjunction with the total particle concentration and FBAP concentration to predict INP concentrations at $T = -20$ °C. Figure S12 summarizes these predictions for the Aug 1-2 and Aug 7-8 samples. For both measurement cycles the prediction underestimates the measured INP concentration. This also holds for $T = -15$ °C and $T = -25$ °C (not shown). We note that Tobo et al. (2013) utilized a different definition of FBAP, one that defined a particle as FBAP if it fluoresced in the band of 420-575 nm when excited by a 355 nm UV source. This excitation-emission value most closely aligns with the WIBS-4A's F3 channel. Using this definition of FBAP would lead to a further underprediction of IN concentration as the particles that fluoresced only in the F3 channel are a subset of the FBAP defined in this study. Additionally, INP concentration parameterizations that are not based on particle concentrations predict concentrations active at -20 °C to be between ~1 L^{-1} (Fletcher 1962) and ~11.5 L^{-1} (Meyers et al 1992).
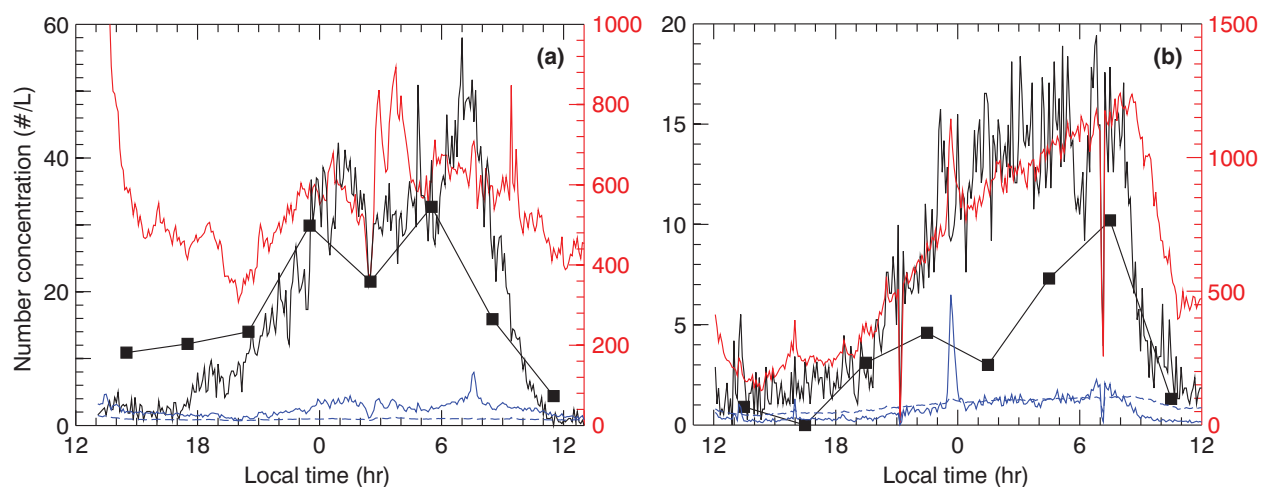
Figure S12. Particle number concentrations over 24 hours starting at (a) August 1, 13:00 and (b) August 7, 12:00 local time. Total measured particle concentration (red solid), total measured fluorescent particle concentration (black solid), and measured IN concentration at T = -20 °C (black squares). Predicted IN concentration active at T = -20 °C using the DeMott et al. (2010) Eq. (1) (blue dashed) and Tobo et al. (2013) (solid blue) are superimposed. Black and blue lines are mapped to the left ordinal axis and red lines are mapped to the right ordinal axis.

References

Banta, R. M., Y. L. Pichugina, and W. A. Brewer (2006), Turbulent Velocity-Variance Profiles in the Stable Boundary Layer Generated by a Nocturnal Low-Level Jet, *Journal of the Atmospheric Sciences*, *63*(11), 2700–2719, doi:10.1175/JAS3776.1.

DeMott, P. J., Prenni, A. J., Liu, X., Kreidenweis, S. M., Petters, M. D., Twohy, C. H., Richardson, M. S., Eidhammer, T., Rogers, D. C. (2010). Predicting global atmospheric ice nuclei distributions and their impacts on climate, *Proceedings of the National Academy of Sciences of the United States of America*, *107*(25), 11217–22. doi:10.1073/pnas.0910818107.

Després, V. R., Huffman, J. A., Burrows, S. M., Hoose, C., Safatov, A. S., Buryak, G., Fröhlich-Nowoisky, J., Elbert, W., Andreae, M. O., Pöschl, U., Jaenicke, R. (2012). Primary biological aerosol particles in the atmosphere: a review, *Tellus B*, 64. doi:10.3402/tellusb.v64i0.15598.

Elder, J. W. (1959), The dispersion of marked fluid in turbulent shear flow, *Journal of Fluid Mechanics*, *5*(04), 544–560, doi:10.1017/S0022112059000374.

Fletcher, N. H. (1962), The Physics of Rainclouds, Cambridge University Press, Cambridge, UK.

Gabey, A. M., Gallagher, M. W., Whitehead, J., Dorsey, J. R., Kaye, P. H., Stanley, W. R. (2010). Measurements and comparison of primary biological aerosol above and below a tropical forest canopy using a dual channel fluorescence spectrometer, *Atmospheric Chemistry and Physics*, *10*(10), 4453–4466. doi:10.5194/acp-10-4453-2010.

Graber, E. R., and Y. Rudich (2006), Atmospheric HULIS: How humic-like are they? A comprehensive and critical review, Atmospheric Chemistry and Physics, 6(3), 729–753, doi:10.5194/acp-6-729-2006.

Hader, J. D., T. P. Wright, and M. D. Petters (2014), Contribution of pollen to atmospheric ice nuclei concentrations, *Atmospheric Chemistry and Physics*, *14*(11), 5433–5449, doi:10.5194/acp-14-5433-2014.

Hill, S. C., Y. Pan, C. Williamson, J. L. Santarpia, and H. H. Hill (2013), Fluorescence of bioaerosols: mathematical model including primary fluorescing and absorbing molecules in bacteria., Optics express, 21(19), 22285–313.

Huffman, J. A., Treutlein, B., Pöschl, U. (2010). Fluorescent biological aerosol particle concentrations and size distributions measured with an Ultraviolet Aerodynamic Particle Sizer (UV-APS) in Central Europe. Atmospheric Chemistry and Physics, 10(7), 3215–3233 doi:10.5194/acp-10-3215-2010.

Huffman, J. A., B. Sinha, R. M. Garland, a. Snee-Pollmann, S. S. Gunthe, P. Artaxo, S. T. Martin, M. O. Andreae, and U. Pöschl (2012), Size distributions and temporal variations of biological aerosol particles in the Amazon rainforest characterized by microscopy and real-time UV-APS fluorescence techniques during AMAZE-08, *Atmospheric Chemistry and Physics*, *12*(24), 11997–12019, doi:10.5194/acp-12-11997-2012.

Huffman, J. A., Prenni, A. J., DeMott, P. J., Pöhlker, C., Mason, R. H., Robinson, N. H., Fröhlich-Nowoisky, J., Tobo, Y., Després, V. R., Garcia, E., Gochis, D. J., Harris, E., Müller-Germann, I., Ruzene, C., Schmid, B., Sinha, B., Day, D. A., Andreae, M. O., Jimenez, J. L., Gallagher, M., Kreidenweis, S. M., Bertram, A. K., Pöschl, U. (2013). High concentrations of biological aerosol particles and ice nuclei during and after rain. Atmospheric Chemistry and Physics, 13(13), 6151–6164. doi:10.5194/acp-13-6151-2013.Huffman, J. A., B. Sinha, R. M. Garland, a. Snee-Pollmann, S. S. Gunthe, P. Artaxo, S. T. Martin, M. O. Andreae, and U. Pöschl (2012), Size distributions and temporal variations of biological aerosol particles in the Amazon rainforest characterized by microscopy and real-time UV-APS fluorescence techniques during AMAZE-08, *Atmospheric Chemistry and Physics*, *12*(24), 11997–12019, doi:10.5194/acp-12-11997-2012.

Kaye, P. H., Stanley, W. R., Hirst, E., Foot, E. V., Baxter, K. L., Barrington, S. J. (2005). Single particle multichannel bio-aerosol fluorescence sensor, *Optics Express*, *13*(10), 3583. doi:10.1364/OPEX.13.003583.

Kumke, M. U., H. G. Löhmannsröben, and T. Roch (1995), Fluorescence spectroscopy of polynuclear aromatic compounds in environmental monitoring, Journal of fluorescence, 5(2), 139–52, doi:10.1007/BF00727531.

Lewitzka, F., and R. Niessner (1995), Application of Time-Resolved Fluorescence Spectroscopy on the Analysis of PAH-Coated Aerosols, Aerosol Science and Technology, 23(3), 454–464, doi:10.1080/02786829508965328.

Lighthart, B., and B. T. Shaffer (1994), Bacterial flux from chaparral into the atmosphere in mid-summer at a high desert location, *Atmospheric Environment*, *28*(7), 1267–1274, doi:10.1016/1352-2310(94)90273-9.

Mesinger, F., et al. (2004), North American Regional Reanalysis: A long-term, consistent, high-resolution climate dataset for the North American domain, as a major improvement upon the earlier global reanalysis datasets in both resolution and accuracy, *BAMS*.

Meyers, M. P., P. J. DeMott, and W. R. Cotton (1992), New Primary Ice-Nucleation Parameterizations in an Explicit Cloud Model, Journal of Applied Meteorology, 31(7), 708–721, doi:10.1175/1520-0450(1992)031<0708:NPINPI>2.0.CO;2.

Nguyen, T. K. V., M. D. Petters, S. R. Suda, and A. G. Carlton (2014), Trends in particle phase liquid water during the Southern Oxidant and Aerosol Study, *Atmospheric Chemistry and Physics Discussions*, *14*(6), 7469–7516, doi:10.5194/acpd-14-7469-2014.

Panne, U., A. Knöller, R. Kotzick, and R. Niessner (2000), On-line and in-situ detection of polycyclic aromatic hydrocarbons (PAH) on aerosols via thermodesorption and laser-induced fluorescence spectroscopy, Fresenius' journal of analytical chemistry, 366(4), 408–14.

Pöhlker, C., Huffman, J. A, Pöschl, U. (2012). Autofluorescence of atmospheric bioaerosols – fluorescent biomolecules and potential interferences, *Atmospheric Measurement Techniques*, *5*(1), 37–71. doi:10.5194/amt-5-37-2012.

Robinson, N. H., Allan, J. D., Huffman, J. A., Kaye, P. H., Foot, V. E., Gallagher, M. (2013). Cluster analysis of WIBS single-particle bioaerosol data, *Atmospheric Measurement Techniques*, 6(2), 337–347. doi:10.5194/amt-6-337-2013.

Saleeby, S. M. and S. C. van den Heever (2013), Developments in the CSU-RAMS Aerosol Model: Emissions, Nucleation, Regeneration, Deposition, and Radiation, *Journal of Applied Meteorology and Climatology*, *52*(12), 2601–2622, doi:10.1175/JAMC-D-12-0312.1.

Salmond, J. A., and I. G. McKendry (2005), A review of turbulence in the very stable nocturnal boundary layer and its implications for air quality, *Progress in Physical Geography*, *29*(2), 171–188, doi:10.1191/0309133305pp442ra.

Seinfeld, J. H., and S. N. Pandis (2006), *Atmospheric Chemistry and Physics: From Air Pollution to Climate Change*, 2nd ed., Wiley-Interscience, New York.

Slinn, W. G. N. (1983), Precipitation scavenging, in *Atmospheric Sciences and Power Production – 1979*, Chapter 11, Division of Biomedical Environmental Research, U.S. Department of Energy, Washington, DC.

Tobo, Y., Prenni, A. J., DeMott, P. J., Huffman, J. A., McCluskey, C. S., Tian, G., Pöhlker, C., Pöschl, U., Kreidenweis, S. M. (2013). Biological aerosol particles as a key determinant of ice nuclei populations in a forest ecosystem, *Journal of Geophysical Research: Atmospheres*, *118*(17), 10,100–10,110. doi:10.1002/jgrd.50801.

Toprak, E., Schnaiter, M. (2013). Fluorescent biological aerosol particles measured with the Waveband Integrated Bioaerosol Sensor WIBS-4: laboratory tests combined with a one year field study, *Atmospheric Chemistry and Physics*, *13*(1), 225–243. doi:10.5194/acp-13-225-2013.

Wang, X., L. Zhang, and M. D. Moran (2010), Uncertainty assessment of current size-resolved parameterizations for below-cloud particle scavenging by rain, *Atmospheric Chemistry and Physics*, *10*(12), 5685–5705, doi:10.5194/acp-10-5685-2010.

Willeke, K., Lin, X., Grinshpun, S. A. (1998). Improved Aerosol Collection by Combined Impaction and Centrifugal Motion, *Aerosol Science and Technology*, *28*(5), 439–456. doi:10.1080/02786829808965536.

Wright, T. P., M. D. Petters, M. D. (2013). The role of time in heterogeneous freezing nucleation, *Journal of Geophysical Research: Atmospheres*, *118*(9), 3731–3743. doi:10.1002/jgrd.50365.

Wright, T. P., Petters, M. D., Hader, J. D. Morton, T., Holder, A. L. (2013). Minimal cooling-rate dependence of ice nuclei activity in the immersion mode, *Journal of Geophysical Research: Atmospheres*, *118*(2), 1–9. doi:10.1002/jgrd.50810.

Young, G. S., and R. H. Johnson (1984), Meso- and Microscale Features of a Colorado Cold Front, *Journal of Climate and Applied Meteorology*, *23*(9), 1315–1325, doi:10.1175/1520-0450(1984)023<1315:MAMFOA>2.0.CO;2.